

Probing Magnetic Helicity in Different Astrophysical Contexts

N. Oppermann, H. Junklewitz, G. Robbers, and T.A. Enßlin

Max Planck Institute for Astrophysics, Karl-Schwarzschild-Str. 1, 85741 Garching, Germany
e-mail: niels@mpa-garching.mpg.de

Received dd Month yyyy / Accepted dd Month yyyy

ABSTRACT

We present a first application of the recently proposed *LITMUS* test for magnetic helicity, as well as a thorough study of its applicability under different circumstances. In order to apply the test to the galactic magnetic field, the newly developed *critical filter* formalism is used to produce an all-sky map of the Faraday depth. The test does not detect helicity in the galactic magnetic field. To understand the significance of this finding, an applicability study is performed, showing that a definite conclusion about the absence of magnetic helicity in the galactic field is not yet reached. This study is conducted via the test's application to simulated observational data. We consider simulations in a flat sky approximation as well as all-sky simulations, both with constant electron densities assumed and with realistic distributions of thermal and cosmic ray electrons. Our results suggest that the *LITMUS* test does indeed perform very well in cases where constant electron densities can be assumed, both in the flat-sky limit and in the galactic setting. Non-trivial distributions of thermal and cosmic ray electrons, however, may complicate the scenario to the point where helicity in the magnetic field can escape detection.

Key words. ISM: magnetic fields - Galaxies: magnetic fields - Methods: data analysis

1. Introduction

Helicity is of utmost interest in the study of astrophysical magnetic fields. Mean field theories for turbulent dynamos operating in the galactic interstellar medium have been successful in explaining the maintenance of the observed magnetic field strengths (e.g. Subramanian 2002). These theories predict helicity to be present on small scales in interstellar magnetic fields. An observational detection or exclusion of helicity in these fields would therefore either strongly suggest the validity of these theories or indicate the existence of some flaws in them.

However, since helicity is a quantity that describes the three-dimensional structure of a magnetic field and most observation techniques produce at best two-dimensional images leading to an informational deficit, it has thus far largely eluded observers.

Previous work on the detection of magnetic helicity in astrophysical contexts has focused mainly on either magnetic fields of specific objects, such as the Sun (see e.g. Zhang 2010, and references therein) or astrophysical jets (cf. e.g. Enßlin 2003; Gabuzda et al. 2004), or cosmological primordial magnetic fields (e.g. Kahniashvili & Ratra 2005; Kahniashvili et al. 2005). One exception is the work of Kahniashvili & Vachaspati (2006), in which the use of charged ultra high energy cosmic rays of known sources is suggested for probing the three-dimensional structure of magnetic fields through which they pass. However, the sources of ultra high energy cosmic rays are not known yet and the applicability of this test is therefore limited.

The *LITMUS* (Local Inference Test for Magnetic fields which Uncovers heliceS) procedure for the detection of magnetic helicity suggested by Junklewitz & Enßlin (submitted) probes the local current helicity density $\mathbf{B} \cdot \mathbf{j}$, which for an ideally conducting plasma becomes

$$\mathbf{B} \cdot \mathbf{j} \propto \mathbf{B} \cdot (\nabla \times \mathbf{B}). \quad (1)$$

Here, the magnetic field is denoted by \mathbf{B} and the electric current density by \mathbf{j} . The test uses measurements of the Faraday

depth and of the polarization direction of synchrotron radiation to probe the magnetic field components along the line of sight and perpendicular to it, respectively. Its simple geometrical motivation should make it applicable in a general setting, provided the aforementioned quantities can be measured. The results depend only on the properties of the magnetic field along a line of sight and are therefore purely local in the two-dimensional sky projection. Our aim is to test this idea on observational as well as on simulated data and thereby determine the conditions under which the test will yield useful results.

This paper is organized as follows. In Sect. 2, the basic equations used in the *LITMUS* test are reviewed. They are applied to observational data describing the galactic magnetic field in Sect. 3, with special emphasis on a sophisticated reconstruction of the Faraday depth, described in Sect. 3.2. Sect. 4 is devoted to a thorough general assessment of the test's reliability. To this end it is applied to simulated observations of increasing complexity. Sect. 4.1 describes the application in a flat sky approximation, whereas Sect. 4.2 examines all-sky simulations, finally arriving at complete simulations of the galactic setting in Sect. 4.2.2, where realistic electron distributions are added. We discuss our results and conclude in Sect. 5.

2. The Helicity Test

For a thorough introduction into the ideas behind the *LITMUS* test, the reader is referred to Junklewitz & Enßlin (submitted). Here, we only summarize the resulting equations.

On the one hand side, synchrotron emission produced by cosmic ray electrons is used to probe the magnetic field component perpendicular to the line of sight. Its polarization is described by the complex field

$$P = Q + iU = |P| e^{2i\chi}, \quad (2)$$

where Q and U are the usual Stokes parameters quantifying the linearly polarized components of the radiation with respect to some orthogonal coordinate system and χ is the polarization angle with respect to the first coordinate direction.

On the other hand, the Faraday depth

$$\phi \propto \int_{\text{LOS}} n_e \mathbf{B} \cdot d\mathbf{l} \quad (3)$$

is used to probe the magnetic field component parallel to the line of sight (LOS).

A helical magnetic field will lead to a gradient of the squared Faraday depth that is parallel to the polarization direction of the synchrotron emission, as was argued in Junklewitz & Enßlin (submitted). In order to compare the directions of the two quantities, this gradient is also formulated as a complex field

$$G = |\nabla\phi^2| e^{2i\alpha}, \quad (4)$$

with

$$\alpha = \arctan \left(\frac{(\nabla\phi^2)_y}{(\nabla\phi^2)_x} \right), \quad (5)$$

where the indices x and y denote its components with respect to the coordinates used. The helicity test that is performed in this work consists simply of multiplying G with the complex conjugate of the polarization P^* . If the two angles χ and α differ by a multiple of π (i.e. the gradient and the polarization direction are parallel), the product will be real and positive. If they differ by an odd multiple of $\pi/2$ (i.e. the two directions are perpendicular), it will be real and negative. Any orientation in between will produce varying real and imaginary parts in the product. Thus, observational directions along which a magnetic field is helical are indicated by a positive real part and a vanishing imaginary part of the product. Averaging over all directions will give an indication of the global helicity of the field.

3. Application to Galactic Observations

In this section, we try to answer the question whether the magnetic field of the Milky Way is helical by applying the *LITMUS* test to the available observational data. Since the magnetic field is localized in a region that surrounds the observer, all relevant quantities will be given as fields on the sphere S^2 , i.e. as functions of the observational direction, specified by two angles ϑ and φ , which are taken to represent the standard spherical polar coordinates in a galactic coordinate system.

3.1. Observational Data

For the synchrotron emission, we use the data gathered by the WMAP satellite after seven years of observations¹, described in Page et al. (2007). Since the foreground synchrotron emission is most intense at low frequencies, we use the measurement in the K-Band, which is centered at a frequency of $\nu = 23$ GHz. Furthermore, we assume that the detected polarized intensity is solely due to galactic synchrotron emission. Thus, the Stokes Q and U parameter maps (defined with respect to the spherical polar coordinate directions \hat{e}_ϑ and \hat{e}_φ in the galactic coordinate system) can be simply combined according to equation (2) to give

¹ The data are available from NASA's Legacy Archive for Microwave Background Data Analysis at <http://lambda.gsfc.nasa.gov>.

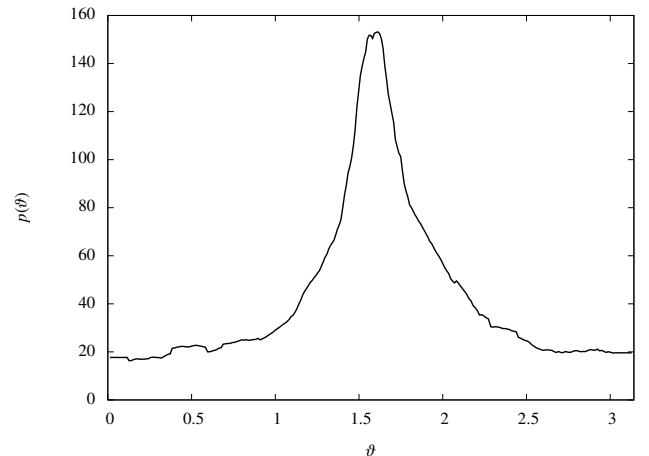


Fig. 1. Vertical galactic profile $p(\vartheta)$ of the Faraday depth.

the complex quantity P whose argument is twice the rotation angle of the plane of polarization with respect to the \hat{e}_ϑ -direction

$$\chi(\vartheta, \varphi) = \frac{1}{2} \arctan \left(\frac{\text{Im}(P(\vartheta, \varphi))}{\text{Re}(P(\vartheta, \varphi))} \right) \quad (6)$$

(cf. Junklewitz & Enßlin submitted).

In order to construct a map of the Faraday depth, we use the catalogue of rotation measurements provided by Taylor et al. (2009)². These provide an observational estimate of the Faraday depth for certain directions in the sky where polarized radio point-sources could be observed. Since the catalogue encompasses a large number (37 543) of point-sources, it paints a rather clear picture of the structure of the Faraday depth. However, earth's shadow prevents observations in a considerably large region within the southern hemisphere.

3.2. Reconstructing the Faraday Depth Map

The reconstruction is conducted according to the *critical filter* method first presented in Enßlin & Frommert (2010). A more elegant derivation of the same filter can be found in Enßlin & Weig (2010). Since this formalism takes into account available information on the statistical properties of the signal in the form of the power spectrum, it is able to interpolate into regions where no direct information on the signal is provided by the data, such as the shadow of earth in this case. Furthermore, it takes into account the available information on the uncertainty of the measurements. All in all it is expected to lead to a reconstructed map of the Faraday depth that is much closer to reality than e.g. a map in which the data were simply smoothed to cover the sphere. Small-scale features that are lost in such a smoothing process are for example reproduced by the *critical filter* algorithm.

3.2.1. Data Model

The field that is to be reconstructed here is the sky-map of the Faraday depth. In order to apply the *critical filter* formula, the signal should be an isotropic Gaussian field. Since the Faraday depth clearly is larger along directions passing through the galactic plane, the condition of isotropy is not satisfied. Therefore, a

² The catalogue is available at <http://www.ucalgary.ca/ras/rmcatatlogue>.

vertical profile is calculated by binning the observations into intervals $[\vartheta_i, \vartheta_i + \Delta\vartheta)$, calculating the root mean square rotation measure value for each bin and smoothing the resulting values to obtain a smooth function $p(\vartheta)$. The result is shown in Fig. 1. This profile is used to approximatively correct the anisotropies induced by the galactic structure and the resulting signal field

$$s(\vartheta, \varphi) = \frac{\phi(\vartheta, \varphi)}{p(\vartheta)} \quad (7)$$

is assumed to be isotropic and Gaussian with a covariance matrix S . The Gaussian covariance matrix is determined solely by the angular power spectrum coefficients C_l , the reconstruction of which is part of the problem at hand.

The data d , i.e. the rotation measure values in the catalogue, are taken to arise from the signal s by multiplication with a response matrix R , which consists of a part encoding the specific directions in which the signal field is probed in order to produce the measurements and another part that is a simple multiplication with the vertical profile $p(\vartheta)$. Additionally, a Gaussian noise component n is assumed with a covariance matrix $N = \text{diag}(\sigma_1^2, \sigma_2^2, \dots)$, where σ_i is the one sigma error bar for the i th measurement in the catalogue, which is also provided. Thus, the data are given by³

$$d = Rs + n = \tilde{R}ps + n \quad (8)$$

Any contribution to the measured data from intrinsic Faraday rotation within the sources is expected to be small and therefore neglected here. It could in principle be included by increasing the σ_i -values appropriately.

3.2.2. Reconstruction Method

In order to reconstruct the mean signal field $m = \langle s \rangle$, where the brackets denote a Gaussian posterior mean, i.e. an average over the posterior probability distribution $\mathcal{P}(s|d, C_l) = \mathcal{G}(s - m, D)$, it is also necessary to reconstruct the angular power spectrum C_l . To do so, the critical filter formulas

$$m = Dj \quad (9)$$

and

$$C_l = \frac{1}{2l+1} \text{tr}((mm^\dagger + D)S_l) \quad (10)$$

are iterated, starting with some initial guess for the power spectrum. Here, the signal covariance matrix is expanded as $S = \sum_l C_l S_l$, where S_l is the projection onto the spherical harmonic components with index l . Furthermore, D is the posterior covariance matrix,

$$D = (S^{-1} + R^\dagger N^{-1} R)^{-1}, \quad (11)$$

and j is the information source term,

$$j = R^\dagger N^{-1} d. \quad (12)$$

The \dagger symbol denotes a transposed and complex conjugated quantity.

Since the critical filter is on the brink of exhibiting a perception threshold (cf. Enßlin & Frommert 2010) and it is generally more desirable to overestimate a power spectrum entering a filter than to underestimate it, the coefficients C_l are subjected to a procedure in which the value of C_l is replaced by

³ The discretized version used in the implementations is $d_i = \sum_j R_{ij} s_j + n_i = \sum_j \tilde{R}_{ij} p_j s_j + n_i$, where the index j determines a pixel on the sphere, so that $s_j = s(\vartheta_j, \varphi_j)$ and $p_j = p(\vartheta_j)$.

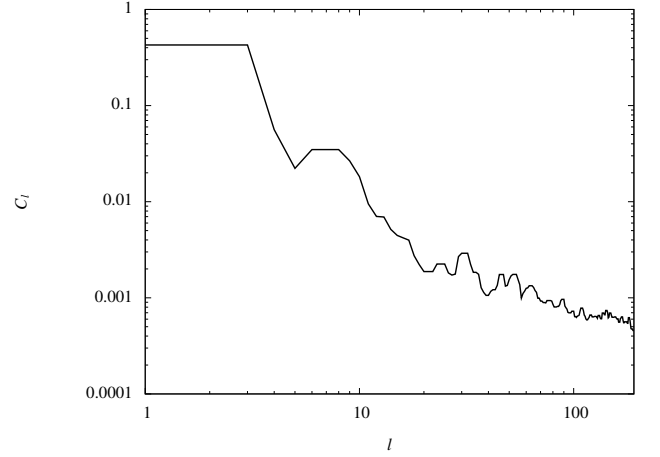


Fig. 3. Angular power spectrum of the signal field s .

$\max\{C_{l-1}, C_l, C_{l+1}\}$ after each iteration step. The advantage of overestimating the power spectrum can be seen by considering the limit of $C_l \rightarrow \infty$ in Eq. (9) and (11). For large values of C_l , the first term in Eq. (11) can be neglected and Eq. (9) becomes

$$m_{C_l \rightarrow \infty} = s + R^{-1}n. \quad (13)$$

Thus, by overestimating the power spectrum the importance of its exact shape is diminished and the reconstruction will instead follow the information given directly by the data more closely. Considering an extreme underestimation of the power spectrum, $C_l \rightarrow 0$, on the other hand, would lead to

$$m_{C_l \rightarrow 0} = 0, \quad (14)$$

suppressing the information given by the data.

3.2.3. Calculating $\nabla\phi^2$

Once the posterior mean of the signal is reconstructed, the corresponding quantity for the squared signal can be calculated according to

$$\langle s^2 \rangle_{\mathcal{G}(s-m, D)} = \langle (m + \psi)^2 \rangle_{\mathcal{G}(\psi, D)} = m^2 + \langle \psi^2 \rangle_{\mathcal{G}(\psi, D)} = m^2 + \hat{D}, \quad (15)$$

where a multivariate Gaussian probability distribution with covariance matrix X is denoted by

$$\mathcal{G}(x, X) = \frac{1}{|2\pi X|^{1/2}} \exp\left(-\frac{1}{2} x^\dagger X^{-1} x\right) \quad (16)$$

and \hat{D} is the vector that contains the diagonal elements of the matrix D .

Thus, given m and \hat{D} , the posterior mean for the Faraday depth is given by $\langle \phi \rangle = pm$, its one sigma error bars by $\pm p\sqrt{\hat{D}}$, and the posterior mean for the desired gradient by

$$\langle \nabla\phi^2 \rangle = \nabla[p^2(m^2 + \hat{D})]. \quad (17)$$

3.3. Results

Figure 2 and 3 summarize the results of the Faraday depth reconstruction and the application of the *LITMUS* test to these data. All calculations are conducted at a HEALPIX⁴ resolution

⁴ The HEALPIX package is available from <http://healpix.jpl.nasa.gov>.

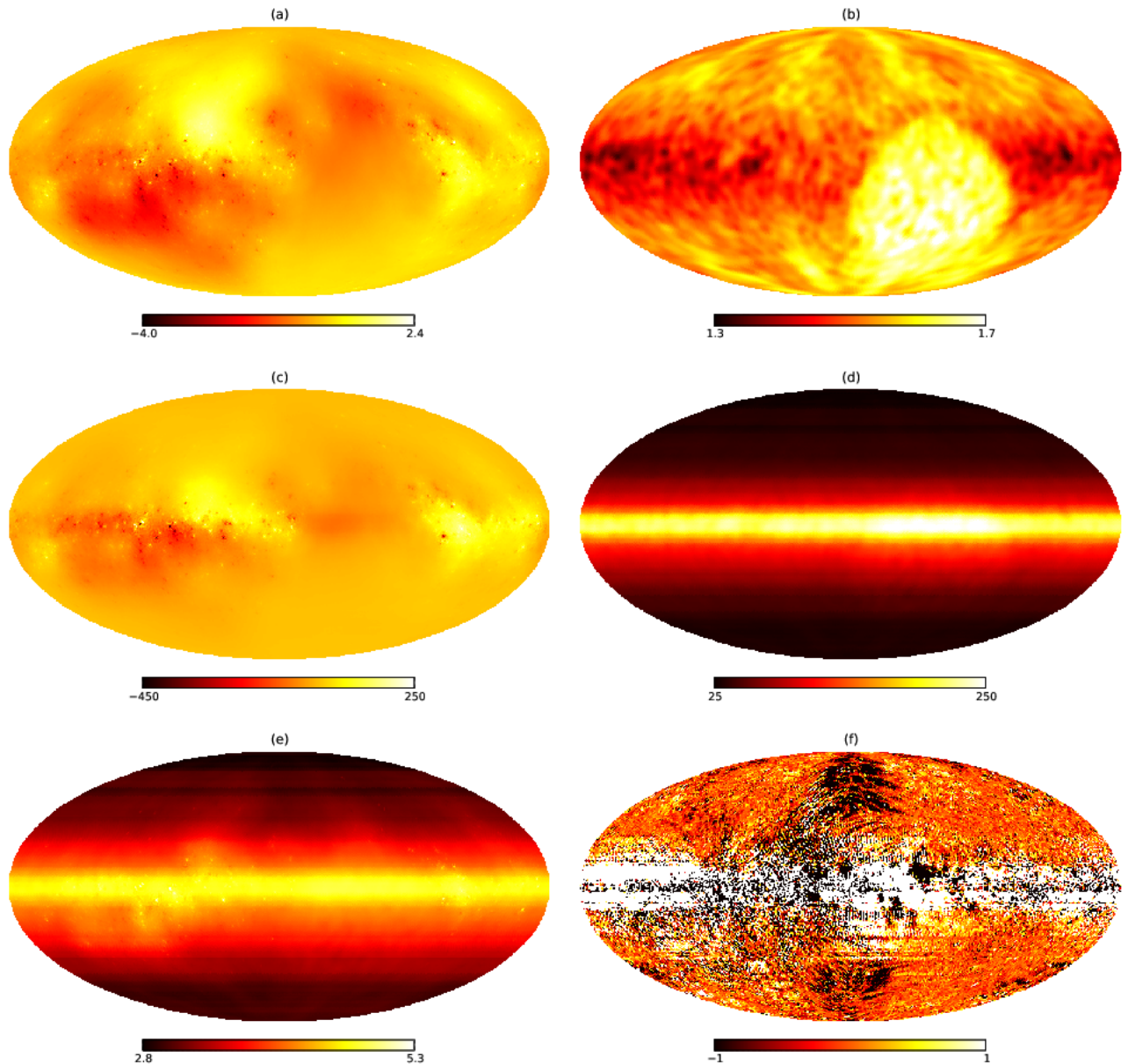


Fig. 2. Results of the Faraday depth reconstruction and the application of the *LITMUS* test to these data. Panel (a) shows the reconstructed signal field s , panel (b) its one-sigma uncertainty. The resulting Faraday depth map is shown in panel (c) and its uncertainty in panel (d). The values are given in m^{-2} . Panel (e) shows the logarithm of the squared Faraday depth map, $\log\left(\left(m/\left[\text{m}^{-2}\right]\right)^2\right)$, where m is the map and m^{-2} its unit, and panel (f) the result of the *LITMUS* test, namely $\text{Re}(GP^*)$, in arbitrary units. The color bar for the last panel does not cover the full range of values.

$N_{\text{side}} = 64$. Figure 3 shows the angular power spectrum of the signal field s which is obtained after the iteration of Eqs. (9) and (10) has converged. In the first panel of Fig. 2, the reconstructed signal field is shown. Evidently, the reconstruction method is able to extrapolate from the available information into regions where no data are taken, i.e. the earth's shadow in the lower right of the projection. However, only structures on scales comparable to the extent of the region without information are reconstructed within it and the reconstruction's uncertainty, shown in panel (b), naturally becomes large in this region. The middle row of Fig. 2 shows the reconstructed Faraday depth and its uncertainty. Clearly, the field $\langle\phi\rangle$ takes on only small values within the information-less region, whereas, again, its uncertainty is especially large there. These two effects add up to yield a field $\langle\phi^2\rangle$, shown in panel (e), that is neither especially small nor especially

large in this region. This is an important fact for the *LITMUS* test, since the gradient of ϕ^2 would otherwise be dramatically contorted near the edge of that region.

Finally, the real part of the product GP^* is shown in the last panel of Fig. 2. Obviously, there is an excess of pixels with a positive value, represented by bright colors, over pixels with a negative value, represented by dark colors, in this image. Indeed, taking the spatial average $\text{Re}\langle GP^*\rangle_{S^2}$ yields a positive value. In order to assess the significance of this value, the two fields G and P are rotated with respect to one another about an angle β around the galactic axis and their product is again averaged over the whole sky. For a helical magnetic field, this procedure should result in a curve $\text{Re}\langle GP^*\rangle_{S^2}(\beta)$ that exhibits a maximum at $\beta = 0$, since the correlations between the fields G and P are expected to be local. The resulting curve for this test is shown in

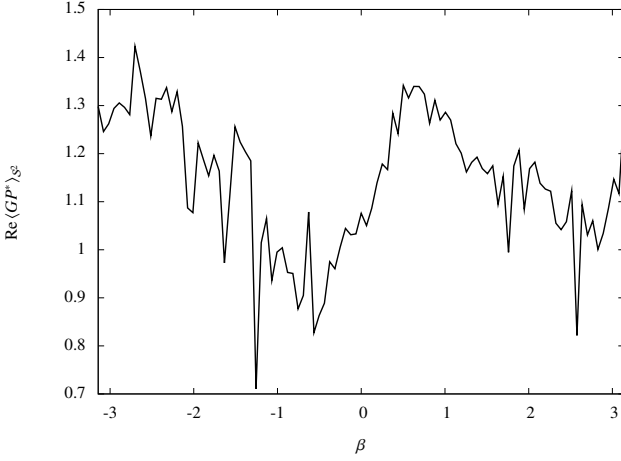


Fig. 4. Rotational curve for $\text{Re}\langle GP^* \rangle_{S^2}$ in arbitrary units.

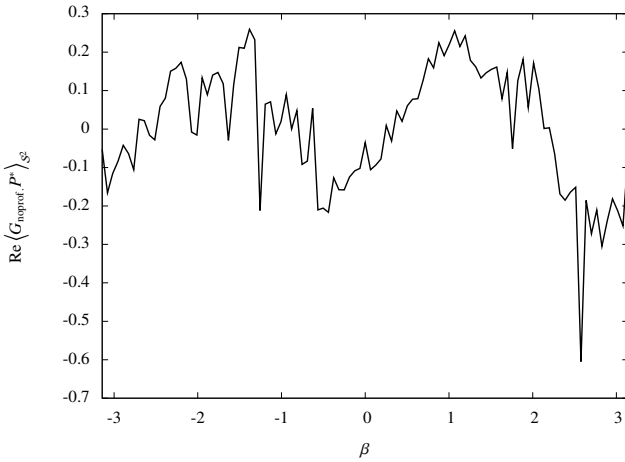


Fig. 5. Same as Fig. 4, only with the factor p^2 dropped in the calculation of ϕ^2 .

Fig. 4. Not only does it not take on its maximum at $\beta = 0$, but it is also clearly positive for any relative rotation between the two fields. Therefore, the positive spatial average can not be counted as a detection of helicity.

A striking feature of Fig. 2.f is the fact that large positive values are encountered mainly within the galactic plane. This can be explained by the vertical galactic profile. Since the absolute value of the Faraday depth tends to be larger the closer the direction is to the galactic plane, there is an overall gradient perpendicular to this plane in $\langle \phi^2 \rangle$. It now happens, due to the magnetic field structure, that the polarization direction of the synchrotron radiation emitted within the galactic plane is also perpendicular to this plane and hence their complex product produces a positive real part, more or less independent of any rotation around the galactic axis.

This explanation can be checked by disregarding the vertical profile, i.e. by dropping the multiplication with p^2 in Eq. (17). In the resulting map of $\text{Re}\langle G_{\text{noprof.}} P^* \rangle$, the positive values around the galactic plane vanish at least partly and the spatial average in fact becomes negative. The rotational curve for this case is shown in Fig. 5. It fluctuates around zero, giving credibility to the assertion that the positive offset in Fig. 4 is due to the galactic profile.

4. Application to Simulated Data

In order to check whether the non-detection of helicity in the previous section allows the conclusion that the galactic magnetic field is in fact non-helical, we now apply the same helicity test to a number of artificially generated magnetic fields with known helicity.

4.1. Planar Implementation

The most simple setting that can be considered is the observation of a well localized magnetic field structure. In the limit of great distances between the magnetic field under consideration and the observer, the lines of sight penetrating the field become parallel. We assume the field to be contained in a cubic box which is oriented along the lines of sight.

The field in the box is generated by the GARFIELDS code (first applied in Kitaura & EnBlin 2008). This code draws the three cartesian components of the magnetic field in Fourier space independently from a common power spectrum, assumed here to be a Kolmogorov-type spectrum of the form $P_B(k) \propto k^{-5/3-2}$, according to Gaussian statistics. In order to produce a magnetic field without divergence, its frequency components parallel to the respective k -vector are then subtracted

$$\mathbf{B}_{\text{div-free}}(\mathbf{k}) \propto \mathbf{B}(\mathbf{k}) - \mathbf{k} \frac{\mathbf{k} \cdot \mathbf{B}(\mathbf{k})}{k^2}. \quad (18)$$

A degree of helicity is then imprinted onto the field by applying the formula

$$\mathbf{B}_{\text{div-free,hel}}(\mathbf{k}) \propto \mathbf{B}_{\text{div-free}}(\mathbf{k}) + \eta \frac{i\mathbf{k} \times \mathbf{B}_{\text{div-free}}(\mathbf{k})}{k}, \quad (19)$$

where $\eta = 0$ leaves the field unaffected and $\eta = \pm 1$ produces the highest degree of helicity.

Finally, we assume the thermal and cosmic ray electron densities to be constant throughout the box. Thus, the observables Q , U , and ϕ can be obtained by simply integrating the appropriate magnetic field components along the box direction associated with the line of sight. Then the complex quantities G and P are easily calculated and multiplied, yielding two-dimensional images of GP^* . This procedure is conducted for various realizations of random magnetic fields both without helicity ($\eta = 0$) and with maximal helicity ($\eta = 1$).

4.1.1. Results

The resulting images for one random magnetic field realization are shown in Fig. 6. The cube was discretized for the calculation into 512^3 pixels. It can already be seen by eye that positive values of $\text{Re}\langle GP^* \rangle$ dominate in the case with maximal helicity (panel (a)), whereas in the case without helicity (panel (b)), positive and negative values seem to be roughly equally represented. Calculating the spatial averages over the whole square yields $\text{Re}\langle GP^* \rangle_{\square} = 4.0 \cdot 10^{-2}$ and $\text{Re}\langle GP^* \rangle_{\square} = 3.6 \cdot 10^{-4}$ for the case with and without helicity, respectively.

We calculated this spatial average for the results of the *LITMUS* test applied to 100 different random magnetic field realizations, both with and without helicity. Averaging these values for the helical fields and for the non-helical fields separately yields a positive value in the helical case. Normalizing all values such that this average becomes equal to one yields

$$\langle \text{Re}\langle GP^* \rangle_{\square} \rangle_{\text{samples}} = 1.0, \quad \sigma_{\text{Re}\langle GP^* \rangle_{\square}} = 0.49$$

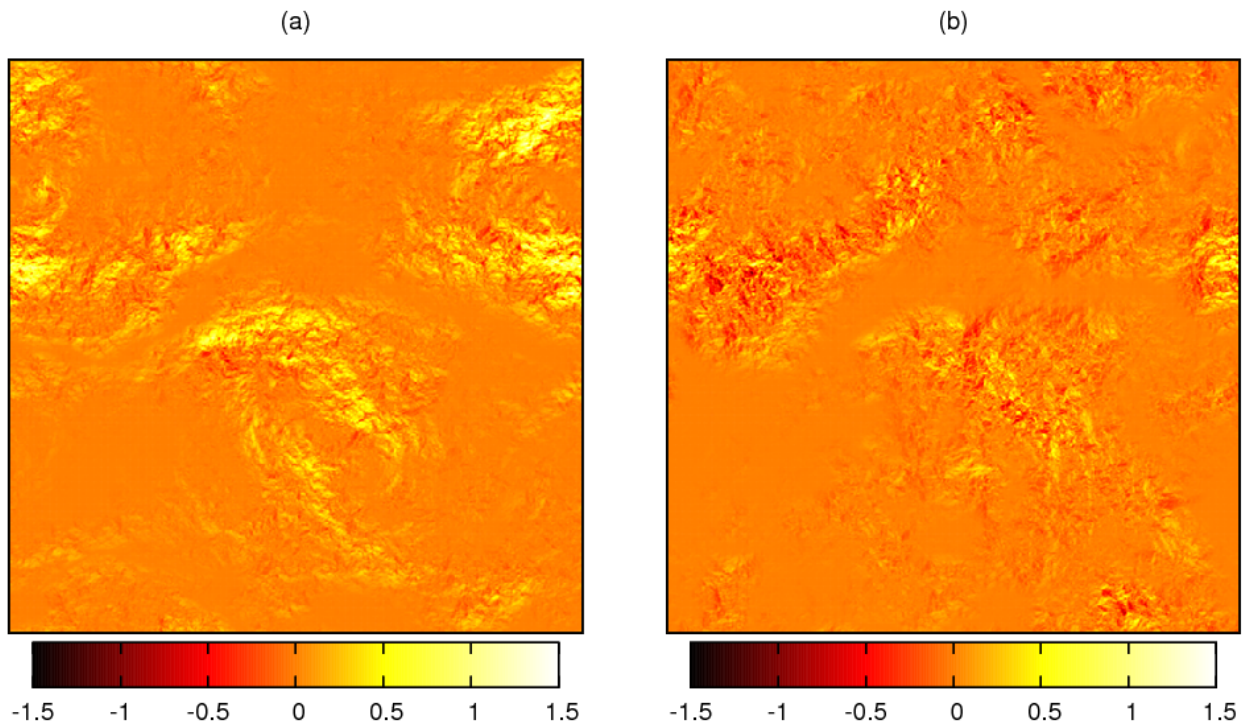


Fig. 6. Maps of $\text{Re}(GP^*)$ for a particular magnetic field realization in arbitrary units. Panel (a) shows the case with maximal helicity ($\eta = 1$), panel (b) the one without helicity ($\eta = 0$).

in the case with helicity and

$$\langle \text{Re}(GP^*) \rangle_{\square} = -0.013, \quad \sigma_{\text{Re}(GP^*)_{\square}} = 0.19$$

in the case without. Clearly, the *LITMUS* test yields positive results if applied to helical fields, whereas its results fluctuate around zero if applied to non-helical fields. This is exactly the behavior that should be expected and the basic functioning of the *LITMUS* test is thereby demonstrated in this setting.

4.2. Spherical Implementation

As a next step, the applicability of the *LITMUS* test is checked for magnetic fields surrounding the observer, as in the case of the galactic field. Again, several sets of mock observations are produced. These simulations are conducted using the *HAMMURABI* code (see Waelkens et al. 2009) in connection with the *GARFIELDS* code⁵. The *HAMMURABI* code allows for a large scale analytic field model and an additional Gaussian random field component, which can be generated by the *GARFIELDS* code with a preset degree of helicity as described in Sect. 4.1.

The *HAMMURABI* code integrates the different field components, weighted with the appropriate electron density, along radial lines of sight and produces sky maps of simulated observations of the Stokes parameters Q and U and Faraday depth ϕ (among others), thus providing all necessary ingredients to perform the *LITMUS* procedure.

4.2.1. Constant Electron Densities

For simplicity, we start again by setting the densities of the thermal electrons and the cosmic ray electrons to constant values throughout the simulated galaxy.

⁵ Both codes are available from <http://www.mpa-garching.mpg.de/hammurabi/hammurabi11>.

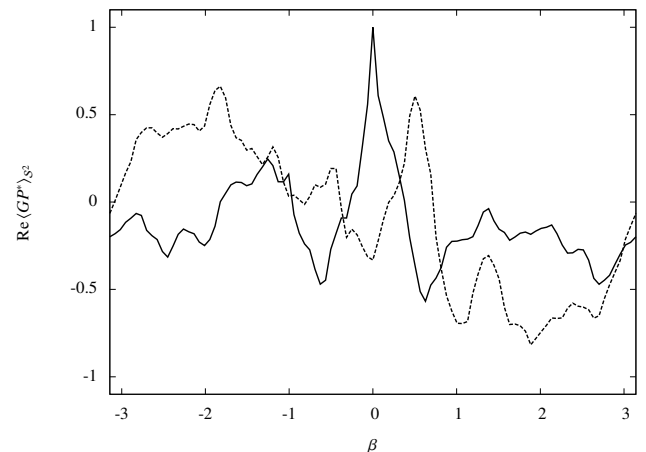


Fig. 7. Rotational curve for $\text{Re}(GP^*)_{S^2}$ in arbitrary units. The solid and dashed lines depict the results for the same magnetic field with helicity parameter $\eta = 1$ and $\eta = 0$ respectively. Constant electron densities are assumed.

Gaussian Random Field. First, in order to apply the test to a field with a well-defined degree of helicity, the field strength of the large scale analytic component is set to zero, such that the simulated galactic field is a purely random one with a chosen degree of helicity. As in the planar case, we choose either no helicity ($\eta = 0$) or maximal helicity ($\eta = 1$).

Figure 7 shows the results of the rotational test described in Sect. 3.3 for one particular Gaussian random magnetic field with a power law index of $-5/3$. Clearly, the spatial average $\text{Re}(GP^*)_{S^2}$ takes on a sharp maximum at $\beta = 0$ and is positive in the case with helicity, while it does not have a maximum there and in fact happens to be negative in the case without helicity. This is exactly the result expected from the *LITMUS* test.

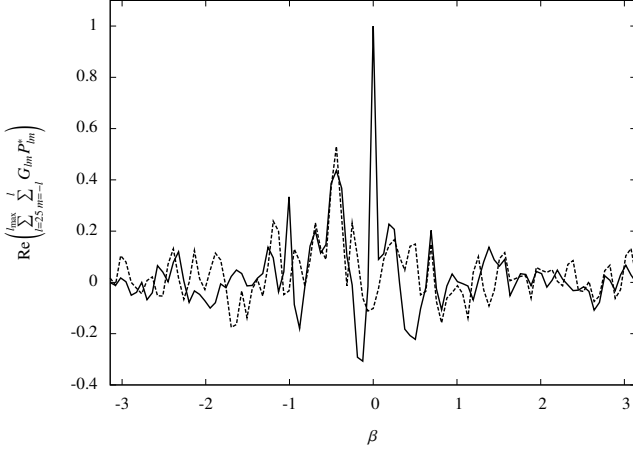


Fig. 8. Same as Fig. 7, only with large-scale contributions neglected.

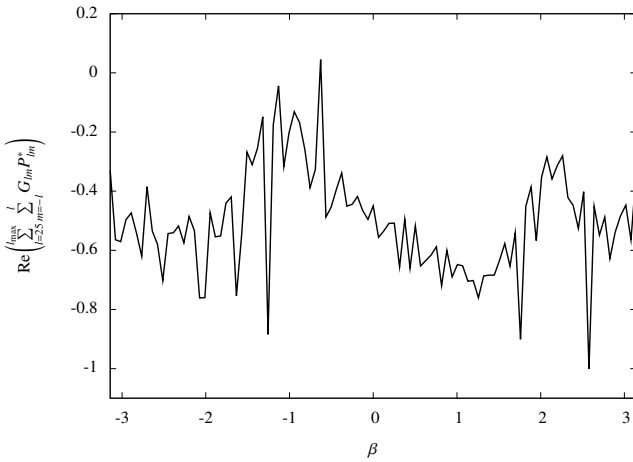


Fig. 9. Same as Fig. 4, only with large-scale contributions neglected.

The sharpness of the peak in Fig. 7 indicates that the helicity is to be found in small-scale features. As a test of this assertion, we calculated the spherical multipole components G_{lm} and P_{lm} of the complex gradient and polarization fields. Note that the spatial average over the product of the fields is proportional to the sum of the products of the multipole components, i.e.

$$\text{Re} \langle GP^* \rangle_{S^2} = \frac{1}{4\pi} \text{Re} \left(\sum_{l=0}^{l_{\max}} \sum_{m=-l}^l G_{lm} P_{lm}^* \right), \quad (20)$$

where l_{\max} is determined by the finite resolution of the map. If we now neglect the first terms in the sum, i.e. the small- l contributions, we arrive at a spatial average over the product in which all large-scale features were neglected. The resulting rotational curves for the same magnetic fields used for Fig. 7 are shown in Fig. 8, where only multipole moments with $l \geq 25$ were considered. It can be seen that this procedure further sharpens the peak at $\beta = 0$ and strengthens it relative to other local maxima in the curves, thus facilitating the detection of small-scale helicity. The same result for the observational data studied in Sect. 3 is shown in Fig. 9. Clearly, there is still no sign of helicity in this case.

Furthermore, we created a set of 100 different Gaussian random magnetic fields, performed the *LITMUS* test, and calculated the spatial average $\text{Re} \langle GP^* \rangle_{S^2}$ for all of them. Each field realization was considered in a version without helicity and a version

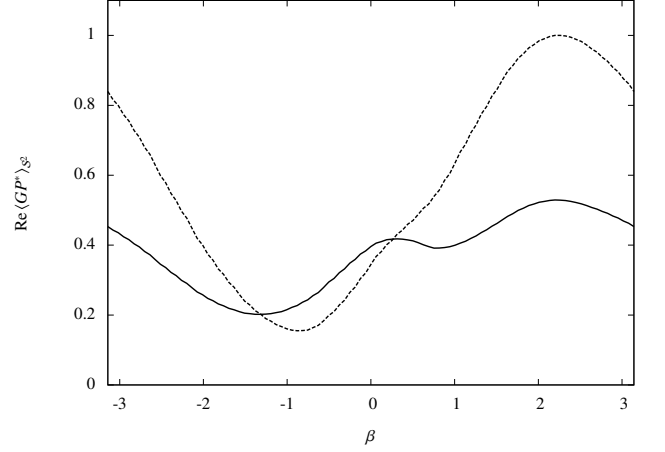


Fig. 10. Rotational curve for $\text{Re} \langle GP^* \rangle_{S^2}$ in arbitrary units. The solid line corresponds to the best-fit magnetic field model of Page et al. (2007), the dashed line to a model where the parameter χ_0 is set to zero. Constant electron densities are assumed.

with maximal helicity, just as in the case of the planar implementation. Averaging over the 100 samples yields again a positive value in the helical case. Normalizing all values such that this average is equal to one yields

$$\langle \text{Re} \langle GP^* \rangle_{S^2} \rangle_{\text{samples}} = 1.0, \quad \sigma_{\text{Re} \langle GP^* \rangle_{S^2}} = 0.72$$

in the helical case and

$$\langle \text{Re} \langle GP^* \rangle_{S^2} \rangle_{\text{samples}} = -0.54, \quad \sigma_{\text{Re} \langle GP^* \rangle_{S^2}} = 0.74$$

in the non-helical case. This clearly underlines the success of the *LITMUS* test in the spherical setting.

Large Scale Field Models. As a next step, the (helical or non-helical) random magnetic field component is switched off completely and replaced by an analytic large scale magnetic field model.

Several sets of simulations are performed using different models for the galactic large scale field. For these analytic models, the current helicity can be calculated directly, giving an expectation as to whether the helicity test should produce positive results or not.

The results of the rotational helicity test are shown in Fig. 10 for the large scale magnetic field model described in Page et al. (2007), i.e.

$$\mathbf{B}(r, \varphi, z) = B_0 \left[\cos(\psi(r)) \cos(\chi(z)) \hat{\mathbf{e}}_r + \sin(\psi(r)) \cos(\chi(z)) \hat{\mathbf{e}}_\varphi + \sin(\chi(z)) \hat{\mathbf{e}}_z \right] \quad (21)$$

in galactic cylindrical coordinates, where

$$\psi(r) = \psi_0 + \psi_1 \ln \left(\frac{r}{8\text{kpc}} \right) \quad (22)$$

and

$$\chi(z) = \chi_0 \tanh \left(\frac{z}{1\text{kpc}} \right). \quad (23)$$

The solid curve corresponds to the parameters favored by Page et al. (2007), namely $\chi_0 = 25^\circ$, $\psi_0 = 27^\circ$, and $\psi_1 = 0.9^\circ$. This corresponds to a simple flat spiral in the galactic plane which

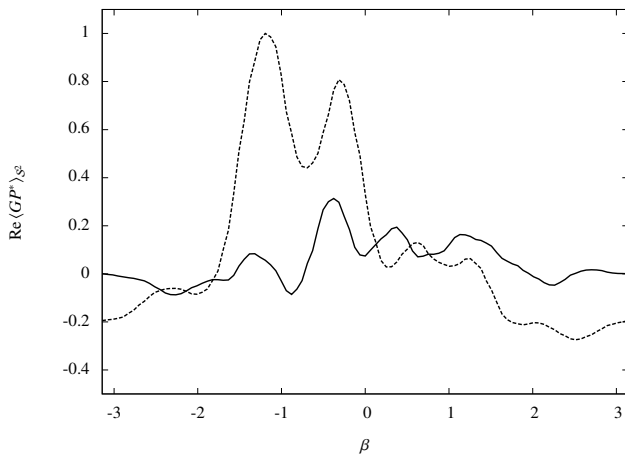


Fig. 11. Same as Fig. 7, only with realistic electron densities used in the calculation.

becomes more and more screw-like with vertical distance z from the galactic plane, so that a slight degree of helicity is inherent in the field geometry. This can be verified by direct calculation according to Eq. (1), yielding

$$\mathbf{j} \cdot \mathbf{B} = B_0^2 \frac{\sin(\chi(z)) \cos(\chi(z))}{r} (\sin(\psi(r)) + \psi_1 \cos(\psi(r))), \quad (24)$$

which is non-zero for any generic point away from the galactic plane. The resulting line in Fig. 10 is *not* a clear indication for this helicity. However, the curve is nevertheless sensitive to the angle χ_0 , which produces the helicity. Lowering its value, i.e. making the spirals more and more parallel to the galactic plane, changes the results of the *LITMUS* test. The extreme case of $\chi_0 = 0$, i.e. $B_z = 0$ everywhere, for which the value of Eq. 24 becomes zero everywhere, is depicted by the dashed line in Fig. 10. This curve's value at $\beta = 0$ is even more distinct from its maximum than in the case of the solid line. This example shows that while the results react in a systematic way on changes in the parameters, the test is not suited to detect helicity on the largest scales.

We used the model of Page et al. (2007) in the demonstration of this effect mainly because of its mathematical simplicity. More sophisticated models can be found e.g. in Jansson et al. (2009), Sun et al. (2008), Jaffe et al. (2010), and references therein.

4.2.2. The Role of the Electron Densities

In order to get closer to a realistic model of the Milky Way, as a next step we replace the constant electron densities with realistic models. The *HAMMURABI* code allows the use of the NE2001 model for the thermal electron density (cf. Cordes & Lazio 2002, 2003) to compute the Faraday depth and several analytic models for the cosmic ray electron density to compute the synchrotron emissivity (see also Waelkens et al. 2009). In the calculations performed to obtain the results presented here, the cosmic ray electron distribution model of Page et al. (2007) was used.

Gaussian Random Field. The resulting rotational curves, as calculated with the realistic electron distributions, for the case of the Gaussian random field are shown in Fig. 11. Neither in the case with helicity ($\eta = 1$), nor in the case without helicity ($\eta = 0$) does the curve take on its maximum at $\beta = 0$. This is

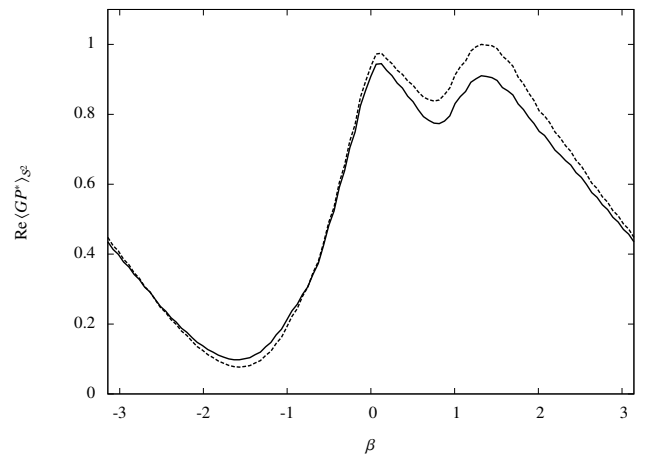


Fig. 12. Same as Fig. 10, only with realistic electron densities used in the calculation.

the expected result in the latter case but contradicts the expectation in the former one. Therefore, the helicity imprinted onto the small scale magnetic field clearly fails to be detected by the test applied.

Large Scale Field Models. The result for the large scale magnetic fields is shown in Fig. 12. There actually seems to be a maximum in the vicinity of $\beta = 0$ now. This is true, however, for the case of the planar spiral model ($\chi_0 = 0$, dashed line in Fig. 12) as well as for the model with helicity ($\chi_0 = 25^\circ$, solid line in Fig. 12). Therefore, the proposed helicity test might under certain circumstances even indicate helicity on large scales where there is none, if the observer is surrounded by the field. Other magnetic field models with planar spirals, such as the bisymmetric (i.e. $\mathbf{B}(r, \varphi, z) = -\mathbf{B}(r, \varphi + \pi, z)$) spiral model of Stanev (1997) lead to similar results.

5. Discussion and Conclusion

The present work presents the first application of the *LITMUS* test for magnetic helicity proposed by Junklewitz & Enßlin (submitted) to actual data. The application of the test involves thoroughly reconstructing a map of the Faraday depth distribution, calculating the gradient G of its square, creating a map of GP^* , averaging over this map, shifting the two fields with respect to each other to see whether any signal vanishes, and filtering out large-scale contributions for a better detection of small-scale helicity. This procedure, applied to observations of the Faraday depth and polarization properties of the synchrotron radiation within our own galaxy in Sect. 3, does not show any signs of helicity in the Milky Way's magnetic field.

In order to assess the significance of this, the applicability of the test was probed in different artificial settings. The complexity of these settings was increased bit by bit to find out under what circumstances exactly the *LITMUS* test yields reliable results.

It was found that meaningful results can be achieved if the electron densities do not vary on the scales of the magnetic field, both in the regime of magnetic field structures whose distance from the observer is much greater than their extension, as shown in Sect. 4.1, and in the regime of magnetic fields surrounding the observer, as shown in Sect. 4.2.1. We showed that the performance of the *LITMUS* test with regard to small-scale helicity is further improved by dropping the first few terms in Eq.

20. However, indications of helicity on large scales are unreliable, as shown in Sect. 4.2.1. Furthermore, it was demonstrated in Sect. 4.2.2 that any non-trivial electron density may distort the outcome of the test to a point where even small-scale helical structures fail to be detected. This is not too surprising since e.g. a variation in the thermal electron density will introduce a gradient in the Faraday depth that is not caused by the magnetic field structure.

Therefore the non-detection of helicity for the galactic magnetic field does not necessarily mean that the field is non-helical on small scales. It may be the case that small-scale fluctuations of the electron density introduce effects in the observational data that prevent the detection of helicity.

So, as a natural next step, the hunt for helicity in astrophysical magnetic fields should focus on a region that is small and/or homogeneous enough for the assumption of constant electron densities to hold at least approximatively.

Although our work has shown that the helicity test that we studied is not suitable for all astrophysical settings, we are confident that it may nevertheless yield useful results if applied in such a setting.

As a side effect of this paper, it was demonstrated in Sect. 3.2 that the method proposed by Enßlin & Frommert (2010) to reconstruct a Gaussian signal with unknown power spectrum is very well suited for practical application.

Acknowledgements. The authors would like to thank Cornelius Weig for help with an efficient planar implementation of the *LITMUS* test. Some of the results in this paper have been derived using the HEALPIX (Górski et al. 2005) package. We acknowledge the use of the Legacy Archive for Microwave Background Data Analysis (LAMBDA). Support for LAMBDA is provided by the NASA Office of Space Science. Most computations were performed using the SAGE software package (Sage 2010). This research was performed in the framework of the DFG Forschergruppe 1254 “Magnetisation of Interstellar and Intergalactic Media: The Prospects of Low-Frequency Radio Observations”. The idea for this work emerged from the very stimulating discussion with Rodion Stepanov during his visit to Germany, which was supported by the DFG–RFBR grant 08-02-92881.

References

- Cordes, J. M. & Lazio, T. J. W. 2002, ArXiv Astrophysics e-prints
 Cordes, J. M. & Lazio, T. J. W. 2003, ArXiv Astrophysics e-prints
 Enßlin, T. A. 2003, A&A, 401, 499
 Enßlin, T. A. & Frommert, M. 2010, ArXiv e-prints
 Enßlin, T. A. & Weig, C. 2010, ArXiv e-prints
 Gabuzda, D. C., Murray, É., & Cronin, P. 2004, MNRAS, 351, L89
 Górski, K. M., Hivon, E., Banday, A. J., et al. 2005, ApJ, 622, 759
 Jaffe, T. R., Leahy, J. P., Banday, A. J., et al. 2010, MNRAS, 401, 1013
 Jansson, R., Farrar, G. R., Waelkens, A. H., & Enßlin, T. A. 2009, J. Cosmology
 Astropart. Phys., 7, 21
 Junklewitz, H. & Enßlin, T. A. submitted
 Kahniashvili, T., Gogoberidze, G., & Ratra, B. 2005, Physical Review Letters,
 95, 151301
 Kahniashvili, T. & Ratra, B. 2005, Phys. Rev. D, 71, 103006
 Kahniashvili, T. & Vachaspati, T. 2006, Phys. Rev. D, 73, 063507
 Kitaura, F. S. & Enßlin, T. A. 2008, MNRAS, 389, 497
 Page, L., Hinshaw, G., Komatsu, E., et al. 2007, ApJS, 170, 335
 Sage. 2010, SAGE Mathematical Software, Version 4.3.3.,
<http://www.sagemath.org>
 Stanev, T. 1997, ApJ, 479, 290
 Subramanian, K. 2002, Bulletin of the Astronomical Society of India, 30, 715
 Sun, X. H., Reich, W., Waelkens, A., & Enßlin, T. A. 2008, A&A, 477, 573
 Taylor, A. R., Stil, J. M., & Sunstrum, C. 2009, ApJ, 702, 1230
 Waelkens, A., Jaffe, T., Reinecke, M., Kitaura, F. S., & Enßlin, T. A. 2009, A&A,
 495, 697
 Zhang, H. 2010, in IAU Symposium, Vol. 264, IAU Symposium, ed.
 A. G. Kosovichev, A. H. Andrei, & J.-P. Roelot, 181–190